

The Earthquake Arrest Zone

Chun-Yu Ke¹, Gregory C. McLaskey¹, David S. Kammer²

¹School of Civil and Environmental Engineering, Cornell University, Ithaca, New York, USA

²Institute for Building Materials, ETH, Zürich, Switzerland

This is a pre-copyedited, author-produced PDF of an article accepted for publication in *Geophysical Journal International* following peer review. The version of record is available online at: <http://doi.org/10.1093/gji/ggaa386>.

Keywords:

- Friction
- Mechanics, theory, and modelling

Abstract

Earthquake ruptures are generally considered to be cracks that propagate as fracture or frictional slip on preexisting faults. Crack models have been used to describe the spatial distribution of fault offset and the associated static stress changes along a fault, and have implications for friction evolution and the underlying physics of rupture processes. However, field measurements that could help refine idealized crack models are rare. Here we describe large-scale laboratory earthquake experiments, where all rupture processes were contained within a 3-m long saw-cut granite fault, and we propose an analytical crack model that fits our measurements. Similar to natural earthquakes, laboratory measurements show coseismic slip that gradually tapers near the rupture tips. Measured stress changes show roughly constant stress drop in the center of the ruptured region, a maximum stress increase near the rupture tips, and a smooth transition in between, in a region we describe as the earthquake arrest zone. The proposed model generalizes the widely used elliptical crack model by adding gradually tapered slip at the ends of the rupture. Different from the cohesive zone described by fracture mechanics, we propose that the transition in stress changes and the corresponding linear taper observed in the earthquake arrest zone are the result of rupture termination conditions primarily controlled by the initial stress distribution. It is the heterogeneous initial stress distribution that controls the arrest of laboratory earthquakes, and the features of static stress changes. We also performed dynamic rupture simulations that confirm how arrest conditions can affect slip taper and static stress changes. If applicable to larger natural earthquakes, this distinction between an earthquake arrest zone (that depends on stress conditions) and a cohesive zone (that depends primarily on strength evolution) has important implications for how seismic observations of earthquake fracture energy should be interpreted.

1 Introduction

The slip profile of an earthquake rupture is the spatial distribution of displacement discontinuity between the fault surfaces, $\delta(x)$. The slip profile of a single earthquake is directly related to the spatial distribution of on-fault stress changes associated with the rupture, $\Delta\tau(x)$. It is therefore important for understanding the mechanics of earthquakes and has implications for stress drop, stress redistribution, and earthquake-to-earthquake triggering (Freed, 2005).

42 Most analytical models of slip profiles are mathematically convenient but can produce
43 physically unrealistic results. Earthquakes are commonly modeled as shear cracks, and
44 the linear elastic crack model (Bilby & Eshelby, 1968) established that a perfect crack
45 with uniform shear stress drop within the rupture area leads to an elliptical slip profile
46 (Fig. 1a). This “elliptical model” casts an infinite stress increase at the rupture tips, which
47 is unrealistic because real interfaces have finite strength. Cowie and Scholz (1992) and
48 Bürgmann et al. (1994) assumed perfectly plastic failure near the rupture tips by adapting
49 the Dugdale (1960) model to a mode II crack. The resulting “bell-shaped” model, shown
50 in Fig. 1a, assumes a constant stress drop inside the ruptured region and a constant stress
51 increase near the rupture tips (Fig. 1c). However, in our experiments, we did not observe a
52 constant stress increase near the rupture tips.

53 Most past field studies of fault slip distributions provide information relevant to the
54 growth of brittle faults over many earthquakes or slow slip events. Studies of faulting showed
55 that slip gradients appeared approximately constant near the fault tip (Muraoka & Kamata,
56 1983; Walsh & Watterson, 1987; Dawers et al., 1993; Nicol et al., 1996; Manighetti et al.,
57 2001), typically 20% of the rupture length (Cowie & Scholz, 1992; Scholz & Lawler, 2004).
58 When considering slip profiles from individual events, measured slip distributions are often
59 so heterogeneous that stacking of many individual events is required to evaluate features.
60 Using this approach, Manighetti et al. (2005) found that slip distributions derived from
61 kinematic models and field observations were roughly triangular and predominantly asym-
62 metric. Walsh and Watterson (1987) argued that the ubiquitous linear tapering feature of
63 slip profiles can be the result of cumulative slips from multiple growing cracks with elliptical
64 shape. This argument highlights the difficulty of distinguishing the field measurements of
65 slip profiles accumulated across multiple earthquake ruptures and of a single earthquake
66 rupture, which will result in very different shapes and possibly different conclusions.

67 Slip at the rupture tips is small and difficult to measure, but can have a strong influence
68 on stress changes. In this work, we use measurements of laboratory earthquakes to illumi-
69 nate the features of earthquake slip profiles, including the area near the rupture tip. We
70 present results from recent large-scale laboratory experiments where the rupture processes
71 are partially or completely contained in a 3-meter long saw-cut granite fault (Ke et al., 2018;
72 Wu & McLaskey, 2019; McLaskey, 2019). This provides a unique opportunity to measure
73 local slip and local static shear stress changes near the tip of an arrested rupture. Similar

74 to observations from natural fault ruptures, we consistently observe slip profiles that taper
75 approximately linearly.

76 In this work, we define the “earthquake arrest zone” as a subsection of an earthquake’s
77 rupture area. It is bounded on one side by the tip of an arrested earthquake rupture. The
78 boundary on the other side is not as clearly defined, but is roughly located where the stress
79 changes that occur during the earthquake $\Delta\tau(x) > \Delta\tau_{\min}$, as shown in Fig. 1d. When a
80 propagating rupture enters the earthquake arrest zone, the rupture front decelerates and
81 ultimately arrests. The elliptical model has an earthquake arrest zone width $w_{\text{az}} = 0$,
82 and the bell-shaped model has a finite w_{az} with constant stress changes within the arrest
83 zone. In our experiments, we find w_{az} on each end of the rupture is approximately 20%
84 of the overall rupture length, and within each earthquake arrest zone we observe stress
85 changes that gradually transition from a peak at the rupture tip to a minimum within the
86 interior of the ruptured region. We propose an analytical crack model that accommodates
87 the aforementioned observations and adheres to physical constraints better than previous
88 models.

89 For each crack model, stress changes can be plotted against slip, as shown in Fig. 1e.
90 Our proposed model produces a relationship that, on first glance, appears to be similar to
91 a linear slip weakening relationship (*e.g.*, Ida, 1972; Palmer & Rice, 1973; Andrews, 1976).
92 However, Fig. 1e shows the final slip and static stress changes at many different locations
93 throughout the earthquake arrest zone, and this is different from a linear slip weakening
94 relationship which describes the evolution of frictional strength as a function of slip at one
95 location on the fault. As will be shown in this work, the earthquake arrest zone is funda-
96 mentally different from the cohesive zone defined in fracture mechanics (*e.g.*, Freund, 1990;
97 Day, Dalguer, Lapusta, & Liu, 2005) due to its physical interpretation. The cohesive zone
98 depends primarily on fault strength evolution (friction), but we will demonstrate that the
99 earthquake arrest zone is produced by the heterogeneous initial stress distribution required
100 to stop the earthquake rupture (see Section 6.3). Section 6.4 presents dynamic rupture sim-
101 ulations that confirm how arrest conditions affect the slip profile and static stress changes
102 during an earthquake (and consequently, the $\Delta\tau$ - δ relationships shown in Fig. 1e) but are
103 largely independent of frictional strength.

104 The difference between a cohesive zone and an earthquake arrest zone has implications
105 for how seismically observed earthquake fracture energy E_G should be interpreted. Here

106 we draw a distinction between E_G —referred to simply as “fracture energy” in seismology,
 107 or “breakdown energy/work” in previous studies (Abercrombie & Rice, 2005; Viesca &
 108 Garagash, 2015; Cocco et al., 2016; Perry et al., 2020)—and Γ the fracture energy normally
 109 used in fracture mechanics (*e.g.*, Andrews, 1976; Day et al., 2005). Γ is a local property
 110 of the material or interface that depends on local strength evolution $\tau_s(\delta)$ according to
 111 $\Gamma = \int_0^\infty [\tau_s(\delta) - \tau_r] d\delta$ (Rice, 1968; Ida, 1972), in which τ_r is the residual strength. (Γ is
 112 a constant in our numerical simulations presented in Section 6.4 that employ linear slip
 113 weakening friction.) E_G is the total strain energy released during the earthquake minus
 114 the radiated energy E_R and the frictional work on the fault plane E_F (Kanamori & Rivera,
 115 2006). It has been assumed that E_G derived from properties of seismic waves can be related
 116 to the strength of the interface or intact rocks (*e.g.*, Abercrombie & Rice, 2005). However, we
 117 suggest that the estimation of E_G can be greatly affected by rupture and arrest properties
 118 and is largely independent of fault strength and Γ .

119 2 Experimental Methods and Measurements

120 Experiments were conducted on a biaxial direct shear apparatus as shown in Fig. 2.
 121 Slip events occurred on the simulated fault as shear load increased. The dimensions of the
 122 moving block and the stationary block are 3.10 m \times 0.81 m \times 0.30 m, and 3.15m \times 0.61 m
 123 \times 0.30 m (respectively) in the x , y , and z directions. The dimensions of the simulated fault
 124 are 3.10 m \times 0.30 m with area $A = 0.95 \text{ m}^2$. The fault surfaces of the granite samples were
 125 prepared by the manufacturer to be flat and parallel to 125 μm . Mechanical properties of
 126 the Barre Gray granite are $E = 30 \text{ GPa}$ and $\nu = 0.23$.

127 The normal loading array, consisting of 18×2 hydraulic cylinders, presses the two rock
 128 blocks together in the y -direction and applies normal contact pressure on the fault. The
 129 shear loading array, consisting of 6×3 hydraulic cylinders, pushes the moving block in
 130 $+x$ -direction and applies shear stress on the fault. Hydraulic cylinders in each array are
 131 interconnected to a manual pump, allowing us to independently control normal and shear
 132 loading. The measurements of hydraulic pressure in both arrays are then converted and
 133 reported as sample average normal and shear stress, $\bar{\sigma}$ and $\bar{\tau}$.

134 Local fault slip was measured by 16 evenly spaced eddy current displacement sensors at
 135 16 locations (E_1 – E_{16}) along the fault as shown in Fig. 2. These sensors measure the relative
 136 displacement between each side of the fault, *i.e.*, the moving rock block and the stationary

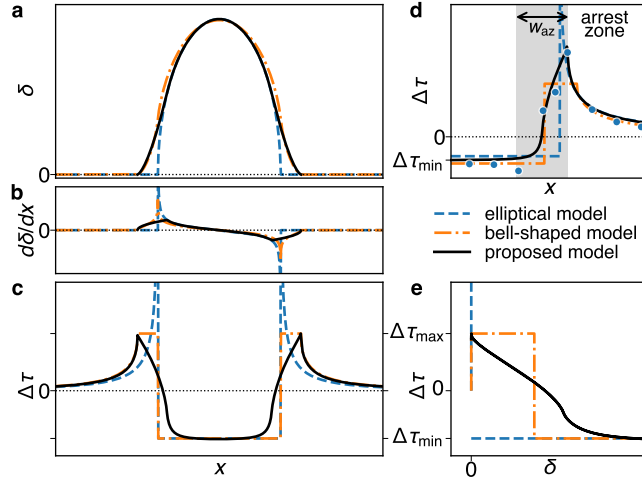


Figure 1. Examples of (a) slip profile $\delta(x)$, (b) first derivative of slip profile $d\delta(x)/dx$, (c) associated shear stress changes $\Delta\tau(x)$. The bell-shaped model is designed to limit the maximum shear stress, casting a constant $\Delta\tau$ plateau near rupture tips under uniform loading and strength field. The proposed model preserves the elliptical slip profile in the center and swaps the edges of the crack with $x^{3/2}$ form, eliminates shear stress singularities, keeps $\Delta\tau(x)$ peaks at rupture tips, and produces a smooth distribution of stress changes with the earthquake arrest zone. (d) a zoom-in of (c) shows the earthquake arrest zone (shaded) in more detail and presents example laboratory measurements (blue dots) of near-fault stress changes with fitted models. w_{az} denotes earthquake arrest zone width. Two distinct data measurements lie inside the earthquake arrest zone where stress changes transition from an apparent maximum level, $\Delta\tau_{max}$, at the crack tip to a minimum level, $\Delta\tau_{min}$, inside the crack. (e) depicts the earthquake stress change versus slip, $\Delta\tau-\delta$, relationship of all three models.

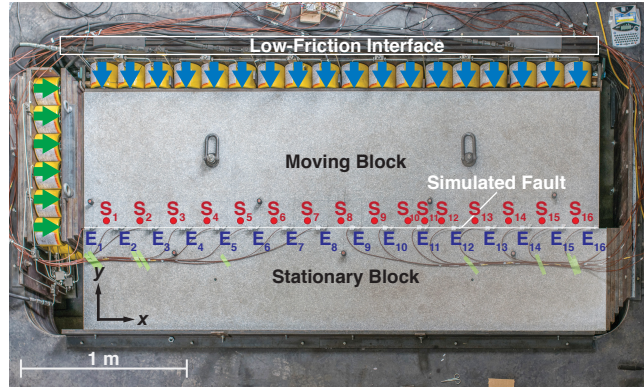


Figure 2. Experimental setup. The moving block and the stationary block were pressed together to compose the simulated fault of granite. A low friction interface consisted of a 2.4 mm thick sheet of reinforced Teflon sliding on precision ground steel plates ($\mu \approx 0.1$) allows the normal loading array (blue arrows) to translate with the moving block in the x -direction. The shear loading array (green arrows) pushes the moving block in the x -direction to apply shear stress and induce ruptures on the simulated fault. S_1 – S_{16} show the locations of 16 sets of strain gage pairs and E_1 – E_{16} show the locations of 16 slip sensors.

137 rock block. Local shear strain was measured by 16 pairs (S_1 – S_{16}) of semiconductor strain
 138 gages at locations shown in Fig. 2, with S_{11} and E_{11} being collocated and all others evenly
 139 spaced between E_1 – E_{16} . Each pair consists of two collocated 4 mm long semiconductor
 140 strain gages oriented at 45° and 135° from the fault which were glued to the moving block,
 141 5 mm from the fault. Local shear stress τ was derived from measurements of the strain gage
 142 pair and the elastic properties of Barre Gray granite. While the 5 mm off-fault measurement
 143 can be biased for dynamic responses (Svetlizky & Fineberg, 2014; Kammer & McLaskey,
 144 2019; Svetlizky et al., 2020), we assume negligible differences between on-fault and 5 mm
 145 off-fault measurements when at (quasi-)static stress states.

146 Before every experiment, we apply $\bar{\sigma} \approx 1$ MPa and then increase τ until the whole sim-
 147 ulated fault slips a few times to create a consistent initial stress distribution for the following
 148 procedures. During the experiments, normal load was first increased to the prescribed level
 149 $\bar{\sigma}_0$ and a valve was closed to keep the volume of hydraulic fluid in the normal loading array
 150 constant. Shear load was then increased at a roughly constant rate to induce sequences of
 151 slip events. Further information about the experimental setup, procedures, and mechanics
 152 of the sequences can be found in Ke et al. (2018) and Wu and McLaskey (2019).

153 In this work, we study individual coseismic slip events. In our experiments, slow fault
 154 creep and nucleation-related slow slip sometimes occurs prior to and after slip events, as
 155 shown in Fig. 3a. For these events, using a smaller time window to calculate δ and $\Delta\tau$ could
 156 exclude quasi-static nucleation process and result in incomplete $\delta(x)$ and $\Delta\tau(x)$, as shown in
 157 Fig. 3b. On the other hand, using a larger time window that includes the nucleation process
 158 and afterslip will also include stress changes from the slow and continuous loading and slip
 159 from quasi-static steady slow slip. We account for these slow processes by fitting linear
 160 trends in time histories before and after the dynamic rupture process then extrapolating
 161 the linear time histories to the instant of the dynamic rupture process and we then take
 162 differences to define the δ and $\Delta\tau$ associated with a dynamic slip event from each location
 163 (Fig. 3). In our experiments, rapid afterslip appears to slightly decrease the stress increase
 164 at the rupture tip of arrested ruptures (not shown), and likely accounts for only a 5% change.
 165 The above procedure lumps the slow slips prior to and after the dynamic rupture to the
 166 changes between the static states before and after the event. Events with fast nucleation
 167 and no afterslip are unaffected.

168 3 Spatial Distribution of Stress Changes

For a mode II (in-plane shear) crack, we define the spatial distribution of shear stress
 change associated with an earthquake rupture as $\Delta\tau(x) \equiv \tau_{\text{f}}(x) - \tau_0(x)$, where $\tau_0(x)$ is the
 spatial distribution of shear stress at the (quasi-)static state before the rupture nucleates and
 $\tau_{\text{f}}(x)$ is the spatial distribution of shear stress at the (quasi-)static state after the rupture
 arrests. Thus, $\Delta\tau(x)$ is the shear stress changes due to all processes of a rupture (nucleation,
 dynamic rupture propagation, and rapid afterslip) between two (quasi-)static states. Bilby
 and Eshelby (1968) derived the constitutive relationship between the distribution of slip
 parallel to the fault $\delta(x)$ and shear stress change distribution $\Delta\tau(x)$,

$$\Delta\tau(x) = -\frac{\mu^*}{2\pi} \int_{a_-}^{a_+} \frac{d\delta(\xi)/d\xi}{x - \xi} d\xi, \quad (1)$$

169 where $\mu^* = \mu/(1 - \nu)$ for mode I and II, $\mu^* = \mu$ for mode III, in which μ is the shear
 170 modulus and ν is the Poisson's ratio, and a_{\pm} are the locations of the rupture tips. This
 171 equation assumes the material surrounding the rupture is linear elastic. It takes the first
 172 derivative of the slip profile $d\delta(x)/dx$ as input and gives its respective static stress change
 173 distribution $\Delta\tau(x)$. Note that if a given $\delta(x)$ is C^1 continuous and $\delta(x) \sim (\pm[a_{\pm} - x])^{3/2}$ as
 174 x approaches a_{\pm} within the rupture, its respective $\Delta\tau(x)$ is smooth and finite (see Uenishi
 175 and Rice (2003): Appendix A).

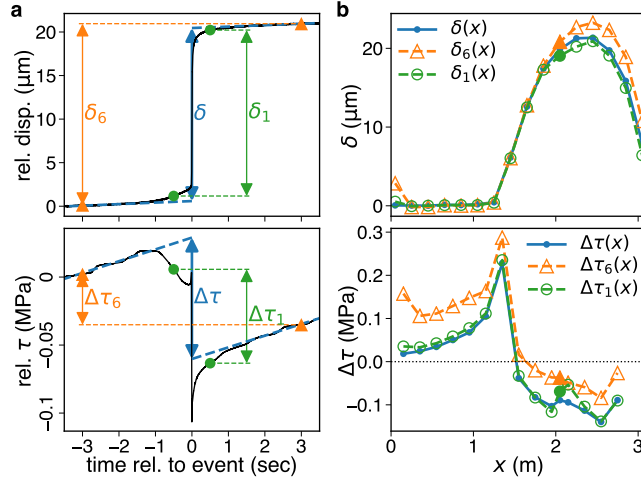


Figure 3. Example of slip and stress change time histories and extracted δ and $\Delta\tau$ from FS01-038-7MPa-P-1-03 event. (a) Heavy dashed lines are linear trends associated with continuous loading and fitted from data before ($t = -3$ to -2 sec) and after ($t = 2$ to 3 sec) the event. Parameters δ and $\Delta\tau$ are then defined by the difference between linear trends before and after the event extrapolated to the instant of dynamic rupture ($t = 0$) as shown. δ_6 and $\Delta\tau_6$ are defined by the difference with a 6-second time window, *i.e.*, difference between $t = \pm 3$ second. Similarly, δ_1 and $\Delta\tau_1$ are defined by the difference with a 1-second time window. (b) Solid curves are results of $\delta(x)$ and $\Delta\tau(x)$ with linear trends removed. Dashed curves are estimates made without linear trends removed. The estimate from a 6-s window, $\delta_6(x)$, is slightly larger than $\delta_1(x)$ due to the inclusion of quasi-static slip during nucleation and after slip. Similarly, $\Delta\tau_6 > \Delta\tau_1(x)$ due to the inclusion of stress changes associated with continuous loading. Note that the deviations near $x = 2$ m in both $\delta_1(x)$ and $\Delta\tau_1(x)$ were due to the exclusion of the quasi-static nucleation process.

176

4 Proposed Crack Model

Our model combines the elliptical shape in the center of the rupture and an $r^{3/2}$ form at the edges, which replaces stress singularities in the elliptical model with mathematically simplistic earthquake arrest zones. The edges of the slip profile are approximately linear (Fig. 1a), consistent with slip profiles obtained from natural faults. The proposed analytical model of slip profiles is formulated as

$$\delta(r) = \begin{cases} D \left[1 - \left(\frac{r}{\lambda a} \right)^2 \right]^{1/2} & , 0 \leq r \leq r^{\text{joint}} \\ \delta^{\text{joint}} \left(\frac{r-a}{r^{\text{joint}}-a} \right)^{3/2} & , r^{\text{joint}} < r \leq a \\ 0 & , a < r \end{cases} \quad (2)$$

177

where r is the distance to the center of the crack, a is the radius of the crack, λ scales a to the radius of the ellipse $a^{\text{ellipse}} = \lambda a$, in which $0 < \lambda < 1$, $r^{\text{joint}} = a(\sqrt{1+3\lambda^2}-1)$ is the radius where $\delta(r)$ switches between elliptical and $r^{3/2}$ form, and $\delta^{\text{joint}} = \delta(r^{\text{joint}})$, as shown in Fig. 4a. Compared to the elliptical (or ellipsoidal) model, $\delta(r) = D \left[1 - \left(\frac{r}{a} \right)^2 \right]^{1/2}$ for $0 \leq r \leq a$, this model introduces only one additional parameter, λ , and guarantees C^1 continuity in $\delta(r)$ and no singularity in the associated stress changes if $0 < \lambda < 1$. Note that this model reduces into the elliptical model if $\lambda = 1$.

178

179

180

181

182

183

We extend the model to an asymmetrical formulation in a one-dimensional coordinate system (x) by introducing a new parameter x_c as the location of the maximum δ and repeating a and λ on either side of x_c ,

$$\delta(x) = \begin{cases} \delta_-^{\text{joint}} \left(\frac{x - x_-^{\text{tip}}}{x_-^{\text{joint}} - x_-^{\text{tip}}} \right)^{3/2} & , x_-^{\text{tip}} < x < x_-^{\text{joint}} \\ D \left[1 - \left(\frac{x-x_c}{\lambda_- a_-} \right)^2 \right]^{1/2} & , x_-^{\text{joint}} \leq x < 0 \\ D \left[1 - \left(\frac{x-x_c}{\lambda_+ a_+} \right)^2 \right]^{1/2} & , 0 \leq x \leq x_+^{\text{joint}} \\ \delta_+^{\text{joint}} \left(\frac{x_+^{\text{tip}} - x}{x_+^{\text{tip}} - x_+^{\text{joint}}} \right)^{3/2} & , x_+^{\text{joint}} < x < x_+^{\text{tip}} \\ 0 & , \text{otherwise} \end{cases} \quad (3)$$

184

185

186

187

188

where x_c is the location of maximum δ such that $\delta(x_c) = D$, a_{\pm} are the rupture half-lengths on either side of x_c , $x_{\pm}^{\text{tip}} = x_c \pm a_{\pm}$ are the locations of rupture tips, λ_{\pm} controls the radius of the ellipse $a_{\pm}^{\text{ellipse}} = \lambda_{\pm} a_{\pm}$, in which $0 < \lambda_{\pm} < 1$, $x_{\pm}^{\text{joint}} = x_c \pm \left(\sqrt{1+3\lambda_{\pm}^2}-1 \right) a_{\pm}$ are the locations where $\delta(x)$ switches between elliptical and $(\pm[a_{\pm}-x])^{3/2}$ forms, and $\delta_{\pm}^{\text{joint}} = \delta(x_{\pm}^{\text{joint}})$, as shown in Fig. 4b.

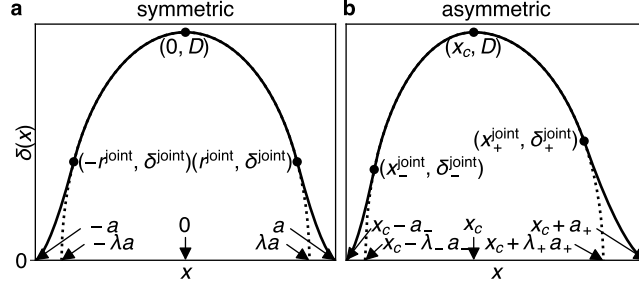


Figure 4. Parameters of the proposed slip profile model in one-dimensional (a) symmetric form (Eqn. 2) and (b) asymmetric form (Eqn. 3). (a) Dotted curve shows the elliptical model this model follows between $\pm r^{\text{joint}}$ with radius λa and height $\delta(0) = D$, in which a is the half-length of the rupture and $0 < \lambda < 1$. (b) Dotted curve shows the asymmetric elliptical model this model follows between x_{\pm}^{joint} with radius $\lambda_{\pm} a_{\pm}$ on either side of x_c , in which x_c is the location such that $\delta(x_c) = D$, $x_c \pm a_{\pm}$ are the locations of rupture tips x_{\pm}^{tip} .

189

5 Results

190

191

192

193

194

195

196

197

198

Fig. 5 shows slip profiles and associated stress changes measured from eight different contained laboratory-generated earthquakes and the respective model fits, where events (1)–(4) are completely contained and events (5)–(8) are partially contained. The spatial resolution of slip profile $\delta(x)$ measurements is arguably not high enough to resolve the fine details near the rupture tips. However, $\Delta\tau(x)$ is very sensitive to the details of $\delta(x)$ non-locally, therefore measurements of $\Delta\tau(x)$ provide additional data to guide and resolve the fine details in $\delta(x)$ near the rupture tips. Simultaneously fitting a model to both $\delta(x)$ measurements and $\Delta\tau(x)$ measurements is a more robust way to resolve $\delta(x)$ and the associated $\Delta\tau(x)$ of earthquake ruptures compared to interpolating between sparse measurements.

199

200

201

202

203

204

205

206

207

Fig. 5b shows two relatively large rupture events (4) and (8) from our experiments to demonstrate the quality of model fits of the elliptical model, the bell-shaped model, and the proposed model. To accommodate the restriction that the bell-shaped model cannot be stretched asymmetrically, we sliced slip profiles in half with respect to the location of maximum δ for the comparison between models. All three models fit $\delta(x)$ well, however, the shapes of $\Delta\tau(x)$ differ near the rupture tip, *i.e.*, in the earthquake arrest zone. Importantly, our $\Delta\tau(x)$ measurements nearly always contain at least one data point with an intermediate value of $\Delta\tau$ located between the maximum $\Delta\tau$ at the rupture tip and the nearly constant $\Delta\tau$ within the central portion of the ruptured region. Even though the spatial resolution

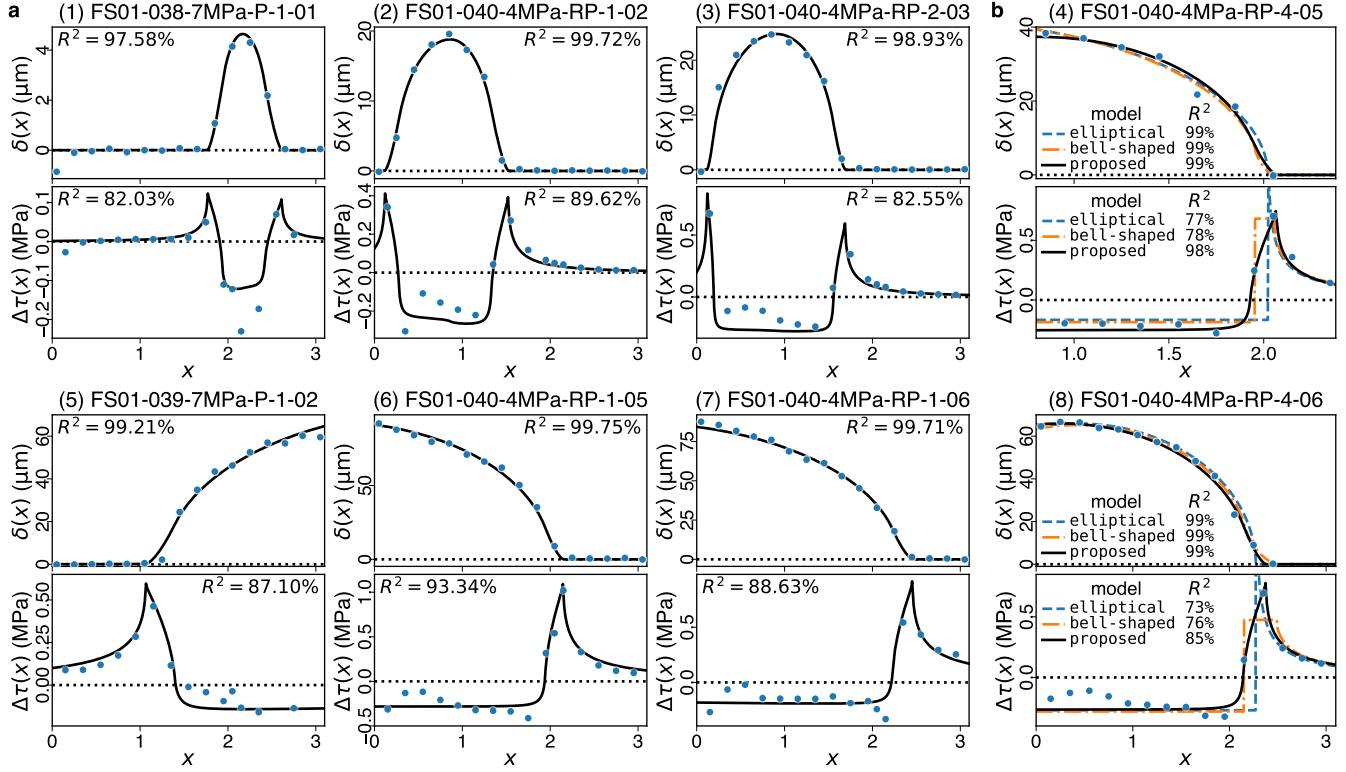


Figure 5. Examples of measured rupture events and model fits of (1)–(4) completely contained and (5)–(8) partially contained laboratory earthquakes. (a) Blue dots indicate measurements of $\delta(x)$ and $\Delta\tau(x)$. Solid curves are results of model fits. The coefficient of determination R^2 of model fits is marked next to each curve. (b) Comparison between the elliptical, the bell-shaped, and the proposed model. Entries in legends denote R^2 of each model fit, where only half of the rupture is shown.

208 of strain measurements is not high enough to verify the exact shape of $\Delta\tau(x)$ within the
 209 earthquake arrest zone, they provide clear evidence of the existence of an earthquake arrest
 210 zone and a smoothly varying $\Delta\tau(x)$ within the arrest zone. The proposed model better
 211 matches our data than the discontinuity in $\Delta\tau(x)$, which is a feature of both the elliptical
 212 model and the bell-shaped model. Of the 24 completely contained ruptures and 13 partially
 213 contained ruptures studied here, the coefficient of determination R^2 of $\delta(x)$ and $\Delta\tau(x)$ fits
 214 are $97.7\% \pm 2.3\%$ and $83.7\% \pm 10.7\%$, respectively.

6 Discussion

6.1 Earthquake arrest zone and comparison between different models

The proposed model merges an elliptical slip profile with a $x^{3/2}$ form at the edges. This allows constant stress drop in the center while keeping the stress concentration at rupture tips finite, and retains a smooth transition in between. The linear tapering feature in slip profiles observed in natural faults is related to the existence of an earthquake arrest zone. Our model's earthquake arrest zone width is $w_{\text{az}} \equiv 2(a - r^{\text{joint}}) = 2a(2 - \sqrt{1 + 3\lambda^2})$, as shown in the shaded area in Fig. 1d. It is the region where $\delta(x)$ is approximately linear and where $\Delta\tau(x)$ transitions from the stress drop within the ruptured region, $\Delta\tau_{\text{min}}$, to the maximum stress increase at the tips of the arrested rupture, $\Delta\tau_{\text{max}}$. The earthquake arrest zone width w_{az} increases with rupture length $2a$ but their ratio $w_{\text{az}}/2a$ is a function of only the shape parameter λ , *i.e.*, $w_{\text{az}}/2a = 2 - \sqrt{1 + 3\lambda^2}$. w_{az} vanishes if $\lambda = 1$ and widens as λ decreases.

The values of λ that best fit laboratory measurements of completely contained ruptures ranged from 0.49 to 0.99, with a median value of 0.85 which reflects $w_{\text{az}}/2a \approx 20\%$, consistent with field observations from larger earthquakes (Cowie & Scholz, 1992; Scholz & Lawler, 2004).

w_{az} in the proposed model is conceptually similar to the friction breakdown zone width of the bell-shaped model (s in Cowie and Scholz (1992), or $a - d$ in Bürgmann et al. (1994)). In the Walsh and Watterson (1987) model, the earthquake arrest zone is essentially the entire rupture half-length. This model also has the approximately linear tapering feature at the edges and limited stress concentration at rupture tips, but its associated stress changes have a fixed triangular shape that does not match our observations or other models that show roughly uniform $\Delta\tau(x)$ inside the ruptured region.

6.2 Scaling of the earthquake arrest zone, earthquake stress drop, and seismically observed earthquake fracture energy E_G

Our experiments produce contained ruptures with half lengths that range from 0.5 m to 2 m. By itself, this provides limited scaling information, and we observe no apparent trend in D or λ against rupture size. However, we gain important insights by imposing some physical constraints supported by field observations of large and small earthquakes.

245 Earthquake ruptures range in size from hundreds of km to hundreds of mm while
 246 absolute strength and fracture energy of the rocks (τ_p, τ_r, Γ) and stress levels of the crust (τ_0)
 247 should remain relatively scale-independent. Note that the apparent peak stress $\Delta\tau_{\max} + \tau_0(x)$
 248 may not represent the actual peak strength of the interface τ_p . We expect $\Delta\tau_{\max}$ to be
 249 bounded by $\tau_p - \tau_0(x)$. Therefore, $\Delta\tau_{\max}$ should also be scale-independent with respect
 250 to rupture size. These constraints agree with the most physically reasonable of the scaling
 251 scenarios considered by Cowie and Scholz (1992). We also assume that the average stress
 252 drop during an earthquake $\overline{\Delta\tau} \propto \mu D/a$ is scale independent, consistent with observations
 253 of large and small earthquakes (*e.g.*, Hanks, 1977; Kanamori, Hiroo and Anderson, 1975;
 254 Baltay, Ide, Prieto, & Beroza, 2011).

To illustrate the scaling mathematically, we analytically calculate $\Delta\tau_{\max}$ and $\Delta\tau_{\min}$ by plugging the slip profile into Eqn. 1 at the rupture tip and at the center. Assuming a symmetric crack, this results in

$$\Delta\tau_{\max} = \Delta\tau(r = a) = \frac{\mu^* D}{2\pi a} \Lambda_p(\lambda), \quad (4)$$

$$\Delta\tau_{\min} = \Delta\tau(r = 0) = -\frac{\mu^* D}{2\pi a} \Lambda_r(\lambda), \quad (5)$$

in which

$$\Lambda_p(\lambda) = -2\frac{\theta}{\lambda} + \frac{3\cos\theta}{\alpha^3} \left[2\alpha - \sqrt{2} \tanh^{-1} \left(\frac{\alpha}{\sqrt{2}} \right) \right] + \frac{2}{\lambda\beta} \left[\tan^{-1} \left(\frac{\lambda + \gamma}{\beta} \right) - \tan^{-1} \left(\frac{\lambda - \gamma}{\beta} \right) \right], \quad (6)$$

$$\Lambda_r(\lambda) = 2\frac{\theta}{\lambda} + \frac{6\cos\theta}{\alpha^3} [\tanh^{-1}(\alpha) - \alpha], \quad (7)$$

255 where $\alpha = \sqrt{1 - \lambda \sin\theta}$, $\beta = \sqrt{1 - \lambda^2}$, $\gamma = \tan(\theta/2)$, and $\theta = \sin^{-1}((\sqrt{1 + 3\lambda^2} - 1)/\lambda)$.
 256 Namely, both $\Delta\tau_{\max}$ and $\Delta\tau_{\min}$ are proportional to μ^* and D/a . The stress ratio $\Delta\tau_{\max}/(-\Delta\tau_{\min})$
 257 = $\Lambda_p(\lambda)/\Lambda_r(\lambda)$ spans $(0, +\infty)$ for $\lambda \in (0, 1)$, monotonically increases as λ increases, and
 258 monotonically decreases as $w_{az}/2a$ increases. This shows that the proposed model can adapt
 259 to arbitrary $\Delta\tau_{\max}$ and $\Delta\tau_{\min}$ as long as $\Delta\tau_{\max} > 0 > \Delta\tau_{\min}$, but might have limitations
 260 fitting both arbitrary stress ratio and arbitrary w_{az} since both depend on λ .

261 Imposing all the above constraints (scale independent D/a , $\Delta\tau_{\max}$, $\Delta\tau_{\min}$, and τ_0) ne-
 262 cessitates a scale invariant λ , which describes a self-similar slip profile, as shown in Fig. 6a.
 263 Note that Fig. 6 shows the scaling relations of independent arrested earthquake ruptures
 264 rather than snapshots of rupture growth. A result of self-similarity is that w_{az} scales with
 265 rupture length ($2a$), as shown in Fig. 6c, and this implies that the seismically observed

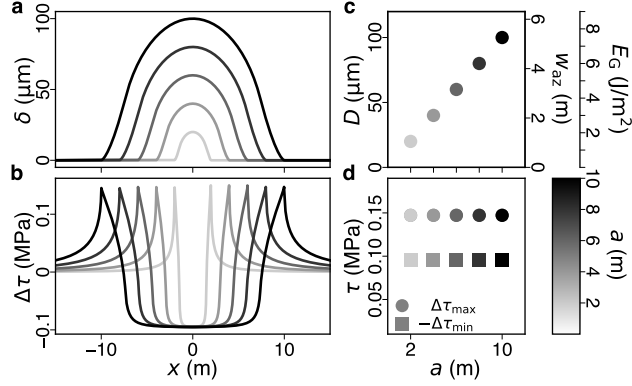


Figure 6. Scaling relations of the proposed model for a from 2 to 10 m. (a) Slip profile $\delta(x)$ of earthquake ruptures of different a and (b) the respective associated stress changes $\Delta\tau(x)$. (c) Scaling relations of maximum slip D , earthquake arrest zone width w_{az} , and seismically observed earthquake fracture energy E_G to a . (d) $\Delta\tau_{\max}$ and $-\Delta\tau_{\min}$ of different a .

266 earthquake fracture energy E_G increases with earthquake size, consistent with seismic ob-
 267 servations (Abercrombie & Rice, 2005). In our model with constant λ , $E_G \propto \delta^{\text{joint}} \propto D$.
 268 Since D/a is also a constant, $E_G \propto a$. Note also that $E_G \propto w_{az}$ since both $w_{az} \propto a$ and
 269 $E_G \propto a$, for fixed λ .

270 The scaling relations described above are not unique to our proposed model; they are
 271 identical to those proposed for the bell-shaped model (Cowie & Scholz, 1992) and similar to
 272 a recent theoretical model of dynamic ruptures (Weng & Ampuero, 2019). The self-similar
 273 scaling is also consistent with the CFTT (constant fault tip taper) model (Scholz & Lawler,
 274 2004; Scholz, 2019), analogous to constant CTOA (crack tip opening angle) model for mode
 275 I fracture (Kanninen & Popelar, 1985). Since our proposed model has a slip profile that is
 276 fairly close to a linear taper, we propose that it can be considered a first order analytical
 277 approximation to the CFTT model.

278 **6.3 Physical mechanisms underlying fault tip taper and earthquake arrest** 279 **zone**

Field evidence shows that fault tip taper increases with stress at the rupture tip (Scholz
 & Lawler, 2004). As a result, earthquakes that rupture a preexisting fault (with lower
 strength) taper more gradually than shear cracks that form new faults. This relationship

can be derived analytically from our proposed model. We define that the fault tip taper

$$FTT \equiv \frac{\delta^{\text{joint}}}{w_{\text{az}}/2} = \frac{D}{a} \frac{\cos \theta}{(1 - \lambda \sin \theta)} \equiv \frac{D}{a} F(\lambda), \quad (8)$$

280 where $\delta^{\text{joint}} = D \cos \theta$, $\theta = \sin^{-1} ((\sqrt{1 + 3\lambda^2} - 1)/\lambda)$, and F is a monotonically increasing
 281 function of λ . If λ is constant, the maximum stress change, the minimum stress change, and
 282 their difference scales positively with FTT since FTT , $\Delta\tau_{\text{max}}$, and $\Delta\tau_{\text{min}}$ are all proportional
 283 to D/a .

284 The linear taper of the slip profile has been thought to be due to inelastic deformation
 285 in the rock volume around the fault tips (Cowie & Scholz, 1992; Bürgmann et al., 1994;
 286 Scholz & Lawler, 2004) possibly over multiple earthquake ruptures (Walsh & Watterson,
 287 1987). However, our laboratory earthquake ruptures exhibit earthquake arrest zones but
 288 show no sign of off-fault damage, suggesting that the features observed in the earthquake
 289 arrest zone can result from either friction processes occurring at the interface, or some other
 290 mechanisms.

291 The approximately linear taper at the edges of $\delta(x)$ and, equivalently, the earthquake
 292 arrest zone observed from $\Delta\tau(x)$ measurements in our experiments is orders of magni-
 293 tude larger than the length-scale of cohesive zones that result from commonly used friction
 294 laws, *e.g.*, slip-weakening friction (Ida, 1972; Palmer & Rice, 1973; Andrews, 1976) and
 295 rate- and state-dependent friction (Dieterich, 1979; Ruina, 1983), which also exhibit slip-
 296 weakening behavior during dynamic rupture propagation (Cocco & Bizzarri, 2002). While
 297 the averaged w_{az} of completely contained rupture events from our experiments was about
 298 0.4 m, fracture mechanics theory (Palmer & Rice, 1973) predicts a cohesive zone width of
 299 $w_{\text{coh}} = 9\pi K^2/[32(\tau_p - \tau_r)^2] = 9\pi E d_0^2/(128\Gamma) \approx 10$ mm with $\Gamma \approx 1$ J/m² (Kammer &
 300 McLaskey, 2019) and $d_0 = 1\mu\text{m}$, which is reasonable for the bare granite surfaces in our ex-
 301 periment. The 5 mm off-fault location of the strain gauges cannot explain this discrepancy.
 302 Furthermore, past experiments where both the top and bottom surfaces of the granite sam-
 303 ple were instrumented with slip sensors showed that ruptures were generally one-directional,
 304 so it is unlikely that 2D effects associated with the 0.3 m thickness of the granite sample
 305 strongly affect our estimates.

306 We argue that the earthquake arrest zone observed in our experiments and the corre-
 307 sponding linear taper that has been mapped in field studies are primarily the result of a
 308 heterogeneous initial stress $\tau_0(x)$ prior to rupture and does not relate directly to the strength
 309 evolution of the interface. Under uniform stress, strength, and fracture energy Γ , fracture

310 mechanics predicts that crack growth will not slow down once it initiates. Therefore, in
 311 order to stop an earthquake rupture, the rupture front must encounter either a barrier with
 312 high fracture energy $\Gamma(x)$ or unfavorable stress conditions, *i.e.*, $\tau_0(x) < \tau_r$. Even though
 313 previous studies (*e.g.*, Abercrombie & Rice, 2005; Viesca & Garagash, 2015; Cocco et al.,
 314 2016; Nielsen et al., 2016) have reported scale-dependent “earthquake fracture energy” E_G ,
 315 $\Gamma(x)$ is considered a scale-independent material or interfacial property (*e.g.*, Day et al.,
 316 2005). We believe that the most likely reason for rupture termination is propagation into
 317 unfavorable stress conditions, at least for earthquakes rupturing preexisting faults (Ke et al.,
 318 2018). This is similar to the idea of rupture interacting with the stress shadow of a previous
 319 earthquake on the same fault (*e.g.*, Gupta & Scholz, 2000). As illustrated by the dynamic
 320 rupture simulations described in section 6.4, we suggest that the $\Delta\tau(x)$ in the earthquake
 321 arrest zone, the $\Delta\tau$ - δ relations of Fig. 1e, and the corresponding linear taper in $\delta(x)$ are the
 322 result of rupture termination conditions and bear little resemblance to the underlying fric-
 323 tion behavior of the material or interface. The stress changes within the earthquake arrest
 324 zone $\Delta\tau(x)$ mainly reflect the transition of $\tau_0(x)$ from above to below τ_r . Large earthquakes
 325 appear to have large w_{az} and large seismically observed fracture energy E_G because they
 326 must propagate further into unfavorable stress conditions to halt rupture. It is possible that
 327 the scale dependency of E_G could result from the scale-dependent earthquake arrest zone
 328 while Γ remains scale-independent.

329 **6.4 Examples of heterogeneous $\tau_0(x)$ as the source of observed earthquake** 330 **arrest zone features**

331 To test the above conjecture that the seismically inferred $\Delta\tau$ - δ relationship can be
 332 the result of heterogeneous $\tau_0(x)$, we simulated fully dynamic rupture propagation and
 333 termination with the spectral boundary integral method (Breitenfeld & Geubelle, 1998) in
 334 two different initial stress distributions $\tau_0(x)$. The first example (Fig 7) has a trapezoidal
 335 $\tau_0(x)$, shown as the black dashed line in Fig 7c, and the resulting slip distribution and stress
 336 changes emulate the features of the earthquake arrest zone that we observed in the laboratory
 337 experiments. The second example (Fig 8) has a boxcar $\tau_0(x)$, shown as the black dashed
 338 line in Fig 8c, to emulate the earthquake arrest zone with a constant stress change. Both
 339 simulations have identical material properties ($E = 30$ GPa, $\nu = 0.23$, $\rho = 2700$ kg/m³) and
 340 linear slip-weakening strength evolution law $\tau_s(\delta)$ with peak strength $\tau_p = 8$ MPa, residual
 341 strength $\tau_r = 6$ MPa, and critical slip distance $d_0 = 1$ μ m. The dynamic rupture is nucleated

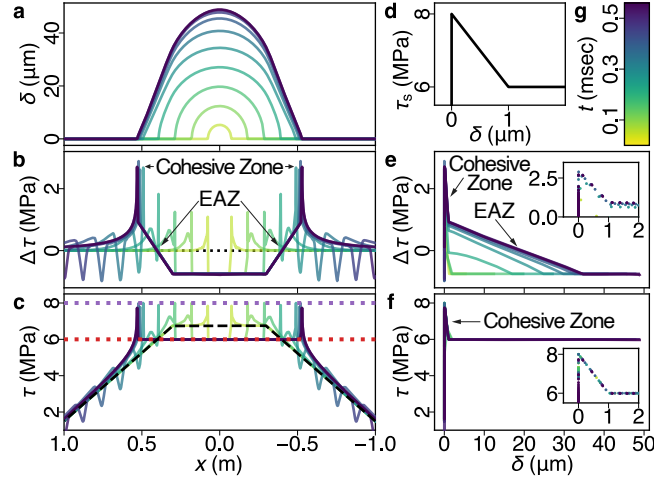


Figure 7. Dynamic simulation of an initial shear stress distribution $\tau_0(x)$ that results in linear slip taper. (a) Snapshots of the slip profile $\delta(x)$, (b) the respective associated stress changes $\Delta\tau(x)$, and (c) the respective absolute stress $\tau(x)$ of the dynamic rupture at different times color coded with (g), in which the opaque dark blue curves represent the static outcomes. Black dashed line in (c) shows a trapezoidal initial stress distribution $\tau_0(x)$. Purple and red dotted lines show the peak strength and the residual strength levels. Oscillations in both (b) and (c) are the shear wave emitted from the nucleation. (d) depicts the imposed strength evolution law $\tau_s(\delta)$. (e) and (f) show the resultant $\Delta\tau$ - δ and τ - δ relationships at different times, respectively. Insets are zoomed in at the spike near $\delta = 0$. The inset in (f) strictly follows $\tau_s(\delta)$ shown in (d). The extent of linear slip taper in (a) coincides with the linear transition from $\Delta\tau_{\min}$ to $\Delta\tau_{\max}$ in (b).

342 by manually extending a seed crack (dropping τ_p to τ_r) bilaterally from $x = 0$ at half the
 343 Rayleigh wave speed until it reaches the critical crack length $L_c \approx 36$ mm and becomes
 344 unstable spontaneously. The rupture front then accelerates towards the Rayleigh wave
 345 speed and decelerates once it propagates into unfavorable stress states, *i.e.*, $\tau_0(x) < \tau_r(x)$.
 346 When the rupture runs out of available strain energy to release, it spontaneously arrests.

347 The difference between Fig. 7e and Fig. 7f, and similarly between Fig. 8e and Fig. 8f,
 348 demonstrates the distinction between the $\Delta\tau$ - δ that can be inferred from earthquake obser-
 349 vations and the underlying frictional strength evolution τ_s - δ relationship. Since the absolute
 350 stress level τ in the Earth is mainly inaccessible, the measured or inferred $\Delta\tau$ from earth-
 351 quakes was sometimes thought to represent the absolute stress level by assuming $\tau_0(x)$ is
 352 uniform across the extent of a rupture. With these two examples, we demonstrated that the
 353 apparent features in $\delta(x)$, such as linear taper or bell-shaped, and in $\Delta\tau$, such as smooth

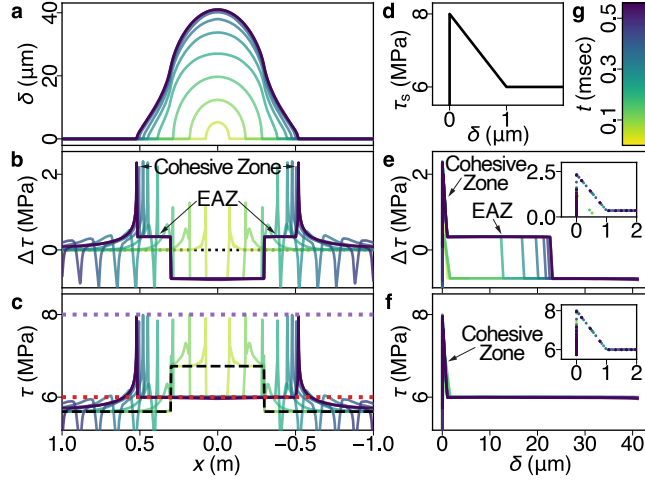


Figure 8. Dynamic simulation of an initial shear stress distribution $\tau_0(x)$ that results in a bell-shaped slip profile. All panels are similar to Fig. 7. Black dashed line in (c) shows a boxcar initial stress distribution $\tau_0(x)$. Note that $\tau_0(x) < \tau_r$ outside the boxcar.

354 transition or a sudden step, can solely result from the shape of the initial stress distribution
 355 $\tau_0(x)$. While the actual cohesive zone is small and hard to measure, the apparent large-scale
 356 feature of $\Delta\tau(x)$ in the arrest zone (Fig 7b) and the apparent slip-weakening feature in the
 357 $\Delta\tau$ - δ curve (Fig 7e) can be produced by the heterogeneous $\tau_0(x)$ and the misrepresentation
 358 of $\Delta\tau$ as τ_s . Similarly, with a crafted $\tau_0(x)$ (Fig 8c), we can emulate a bell-shaped slip
 359 profile (Fig 8a) with linear elasticity (and no off-fault damage).

360 6.5 Smooth observed slip profile

361 Our contained laboratory-generated earthquakes have smoother slip profiles compared
 362 to natural earthquakes. This could be because the simulated fault is more smooth and flat
 363 than natural faults. Another possibility is that our experiments produced “baby” earth-
 364 quakes that reached unfavorable stress conditions and terminated soon after nucleating and
 365 before the rupture front was fully dynamic (Svetlizky et al., 2017), and therefore more com-
 366 plex high-speed processes could not engage. Measurements of $\Delta\tau(x)$ inside the ruptured
 367 region, where dynamic rupture propagation took place, were slightly more deviated from
 368 the model and less smooth compared to the rest of the fault, as shown in Fig. 5. Perhaps the
 369 ruptures are not completely homogeneous along depth while the strain gages are glued on
 370 the surface of the rock blocks, or some randomness is introduced by the rapid fluctuations

371 in slip and stress during the dynamic rupture process as seen in a previous study with a
 372 similar experimental setup (McLaskey et al., 2015).

373 7 Conclusions

374 Our contained laboratory-generated earthquakes ruptured a nominally flat and smooth
 375 frictional interface free from heterogeneities in geometry and material properties. We found
 376 that heterogeneity in initial stress distribution was sufficient to generate laboratory earth-
 377 quakes that terminated within the 3-meter long simulated fault, providing a rare opportu-
 378 nity to study the features of slip profiles and the associated stress changes in a simplified
 379 laboratory setting. In addition to local slip measurements, we used local shear strain mea-
 380 surements to help resolve the details of slip profiles near the rupture tips, where stress
 381 changes are profound. Near the rupture tips, we consistently observe an earthquake arrest
 382 zone where stress changes smoothly transition from the maximum level at the crack tip to
 383 the minimum level within the ruptured region. The earthquake arrest zone was 0.06 m to
 384 0.95 m in size and was, on average, about 20% of the overall rupture length, consistent
 385 with field observations of constant slip gradients (Cowie & Scholz, 1992; Scholz & Lawler,
 386 2004). However the size of the arrest zone we observe is orders of magnitude larger than
 387 the cohesive zone predicted by fracture mechanics theory, using reasonable values of friction
 388 parameters. This leads us to believe that the observed features in the arrest zone are primar-
 389 ily produced by the heterogeneous initial stress distribution required to stop an earthquake
 390 rupture rather than the fault strength. Using a set of numerical simulations of spontaneous
 391 dynamic rupture propagation and termination, we illustrated how an earthquake’s stress
 392 change versus slip relationship ($\Delta\tau-\delta$) inferred from static stress changes can be profoundly
 393 different from the underlying frictional strength evolution ($\tau_s-\delta$). This has profound impli-
 394 cations for how seismically derived estimates of certain earthquake parameters should be
 395 interpreted: The seismically inferred increase in fracture energy E_G and critical slip distance
 396 d_0 with increasing earthquake size (*e.g.*, Abercrombie & Rice, 2005) reflects the manner in
 397 which earthquake ruptures arrest rather than the way fault strength evolves with slip.

398 We propose a slip profile model that does not contain the stress singularity of the
 399 elliptical model; it has an earthquake arrest zone that moderates stress changes at the
 400 rupture tip. Different from previous models that also include an earthquake arrest zone, such
 401 as the bell-shaped model (Cowie & Scholz, 1992; Bürgmann et al., 1994), our proposed model
 402 features smoothly varying stress changes that are more compatible with our laboratory

403 measurements, and this facilitates the interpretation of the extent of the earthquake arrest
 404 zone that is otherwise difficult to define. While the full details of the stress changes within the
 405 earthquake arrest zone are not resolved due to limited spatial resolution in our experimental
 406 measurements, the inferred model provides a proper first-order approximation to the smooth
 407 transition from the maximum to the minimum level through a mathematically simple and
 408 numerically stable formulation of the slip profile. Constrained by physical measurements,
 409 the model may be useful as a component of more complicated fault rupture and rupture
 410 sequence earthquake models.

411 **Acknowledgments**

412 This research was supported by the National Science Foundation under grant EAR-1763499.
 413 Data used in this paper were acquired during laboratory experiments conducted at Cornell
 414 University. Data reported here are publicly available at <https://eCommons.cornell.edu>. We
 415 thank C. Scholz for a helpful review that stimulated transformative changes to this paper.
 416 We thank H. Weng, and two anonymous reviewers for their helpful reviews. We thank Bill
 417 S. Wu for assistance with the experiments. The authors declare that they have no conflict
 418 of interest.

419 **References**

- 420 Abercrombie, R. E., & Rice, J. R. (2005). Can observations of earthquake scaling constrain
 421 slip weakening? *Geophysical Journal International*, *162*(2), 406–424. doi: 10.1111/
 422 j.1365-246X.2005.02579.x
- 423 Andrews, D. J. (1976). Rupture propagation with finite stress in antiplane strain. *Journal*
 424 *of Geophysical Research*, *81*(20), 3575. doi: 10.1029/JB081i020p03575
- 425 Baltay, A., Ide, S., Prieto, G., & Beroza, G. (2011). Variability in earthquake stress
 426 drop and apparent stress. *Geophysical Research Letters*, *38*(6), 1–6. doi: 10.1029/
 427 2011GL046698
- 428 Bilby, B. A., & Eshelby, J. D. (1968). Dislocations and the theory of fracture. In H. Liebowitz
 429 (Ed.), *Fracture, an advanced treatise* (Vol. I, pp. 99–182). San Diego, Calif.: Aca-
 430 demic.
- 431 Breitenfeld, M. S., & Geubelle, P. H. (1998). Numerical analysis of dynamic debonding
 432 under 2D in-plane and 3D loading. *International Journal of Fracture*, *93*(1/4), 13–38.
 433 doi: 10.1023/A:1007535703095

- 434 Bürgmann, R., Pollard, D. D., & Martel, S. J. (1994). Slip distributions on faults: effects
435 of stress gradients, inelastic deformation, heterogeneous host-rock stiffness, and fault
436 interaction. *Journal of Structural Geology*, *16*(12), 1675–1690. doi: 10.1016/0191
437 -8141(94)90134-1
- 438 Cocco, M., & Bizzarri, A. (2002). On the slip-weakening behavior of rate- and state
439 dependent constitutive laws. *Geophysical Research Letters*, *29*(11), 11–1–11–4. doi:
440 10.1029/2001GL013999
- 441 Cocco, M., Tinti, E., & Cirella, A. (2016). On the scale dependence of earthquake stress drop.
442 *Journal of Seismology*, *20*(4), 1151–1170. Retrieved from [http://link.springer](http://link.springer.com/10.1007/s10950-016-9594-4)
443 [.com/10.1007/s10950-016-9594-4](http://link.springer.com/10.1007/s10950-016-9594-4) doi: 10.1007/s10950-016-9594-4
- 444 Cowie, P. A., & Scholz, C. H. (1992). Physical explanation for the displacement-length
445 relationship of faults using a post-yield fracture mechanics model. *Journal of Structural*
446 *Geology*, *14*(10), 1133–1148. doi: 10.1016/0191-8141(92)90065-5
- 447 Dawers, N. H., Anders, M. H., & Scholz, C. H. (1993). Growth of normal faults:
448 Displacement-length scaling. *Geology*, *21*(12), 1107. doi: 10.1130/0091-7613(1993)
449 021<1107:GONFDL>2.3.CO;2
- 450 Day, S. M., Dalguer, L. A., Lapusta, N., & Liu, Y. (2005). Comparison of finite difference
451 and boundary integral solutions to three-dimensional spontaneous rupture. *Journal*
452 *of Geophysical Research: Solid Earth*, *110*(12), 1–23. doi: 10.1029/2005JB003813
- 453 Dieterich, J. H. (1979). Modeling of rock friction: 1. Experimental results and consti-
454 tutive equations. *Journal of Geophysical Research*, *84*(B5), 2161. doi: 10.1029/
455 JB084iB05p02161
- 456 Dugdale, D. (1960). Yielding of steel sheets containing slits. *Journal of the Mechanics and*
457 *Physics of Solids*, *8*(2), 100–104. doi: 10.1016/0022-5096(60)90013-2
- 458 Freed, A. M. (2005). Earthquake Triggering By Static, Dynamic, and Postseismic Stress
459 Transfer. *Annual Review of Earth and Planetary Sciences*, *33*(1), 335–367. doi:
460 10.1146/annurev.earth.33.092203.122505
- 461 Freund, L. B. (1990). *Dynamic Fracture Mechanics* (Vol. 25) (No. 9). Cambridge: Cam-
462 bridge University Press. doi: 10.1017/CBO9780511546761
- 463 Gupta, A., & Scholz, C. H. (2000). A model of normal fault interaction based on obser-
464 vations and theory. *Journal of Structural Geology*, *22*(7), 865–879. doi: 10.1016/
465 S0191-8141(00)00011-0
- 466 Hanks, T. C. (1977). Earthquake stress drops, ambient tectonic stresses and stresses that

- 467 drive plate motions. *pure and applied geophysics: pageoph*, 115(1-2), 441.
- 468 Ida, Y. (1972). Cohesive force across the tip of a longitudinal-shear crack and Griffith's
469 specific surface energy. *Journal of Geophysical Research*, 77(20), 3796–3805. doi:
470 10.1029/JB077i020p03796
- 471 Kammer, D. S., & McLaskey, G. C. (2019). Fracture energy estimates from large-scale
472 laboratory earthquakes. *Earth and Planetary Science Letters*, 511, 36–43. doi: 10
473 .1016/j.epsl.2019.01.031
- 474 Kanamori, H., & Rivera, L. (2006). Energy partitioning during an earthquake. *Geophysical*
475 *Monograph Series*, 170, 3–13. doi: 10.1029/170GM03
- 476 Kanamori, Hiroo and Anderson, D. L. (1975). Theoretical basis of some empirical relations
477 in seismology. *Bulletin of the Seismological Society of America*, 65(5), 1073–1095.
- 478 Kanninen, M. F., & Popelar, C. H. (1985). *Advanced Fracture Mechanics*. Oxford University
479 Press.
- 480 Ke, C.-Y., McLaskey, G. C., & Kammer, D. S. (2018). Rupture Termination in Laboratory-
481 Generated Earthquakes. *Geophysical Research Letters*, 45(23), 12784–12792. doi:
482 10.1029/2018GL080492
- 483 Manighetti, I., Campillo, M., Sammis, C., Mai, P. M., & King, G. (2005). Evidence for self-
484 similar, triangular slip distributions on earthquakes: Implications for earthquake and
485 fault mechanics. *Journal of Geophysical Research*, 110(B5), B05302. doi: 10.1029/
486 2004JB003174
- 487 Manighetti, I., King, G. C. P., Gaudemer, Y., Scholz, C. H., & Doubre, C. (2001). Slip
488 accumulation and lateral propagation of active normal faults in Afar. *Journal of Geo-*
489 *physical Research: Solid Earth*, 106(B7), 13667–13696. doi: 10.1029/2000JB900471
- 490 McLaskey, G. C. (2019). Earthquake Initiation From Laboratory Observations and Im-
491 plications for Foreshocks. *Journal of Geophysical Research: Solid Earth*, 124(12),
492 12882–12904. doi: 10.1029/2019JB018363
- 493 McLaskey, G. C., Kilgore, B. D., & Beeler, N. M. (2015). Slip-pulse rupture behavior on
494 a 2 m granite fault. *Geophysical Research Letters*, 42(17), 7039–7045. doi: 10.1002/
495 2015GL065207
- 496 Muraoka, H., & Kamata, H. (1983). Displacement distribution along minor fault traces.
497 *Journal of Structural Geology*, 5(5), 483–495. doi: 10.1016/0191-8141(83)90054-8
- 498 Nicol, A., Watterson, J., Walsh, J. J., & Childs, C. (1996). The shapes, major axis ori-
499 entations and displacement patterns of fault surfaces. *Journal of Structural Geology*,

- 500 18(2-3), 235–248. doi: 10.1016/S0191-8141(96)80047-2
- 501 Nielsen, S., Spagnuolo, E., Smith, S. A., Violay, M., Di Toro, G., & Bistacchi, A. (2016).
502 Scaling in natural and laboratory earthquakes. *Geophysical Research Letters*, 43(4),
503 1504–1510. doi: 10.1002/2015GL067490
- 504 Palmer, A. C., & Rice, J. R. (1973). The Growth of Slip Surfaces in the Progressive Failure of
505 Over-Consolidated Clay. *Proceedings of the Royal Society A: Mathematical, Physical
506 and Engineering Sciences*, 332(1591), 527–548. doi: 10.1098/rspa.1973.0040
- 507 Perry, S. M., Lambert, V., & Lapusta, N. (2020). Nearly Magnitude-Invariant Stress
508 Drops in Simulated Crack-Like Earthquake Sequences on Rate-and-State Faults with
509 Thermal Pressurization of Pore Fluids. *Journal of Geophysical Research: Solid Earth*,
510 125(3). doi: 10.1029/2019JB018597
- 511 Rice, J. R. (1968, jun). A Path Independent Integral and the Approximate Analysis
512 of Strain Concentration by Notches and Cracks. *Journal of Applied Mechanics*,
513 35(2), 379–386. Retrieved from [https://asmedigitalcollection.asme.org/
514 appliedmechanics/article/35/2/379/392117/A-Path-Independent-Integral
515 -and-the-Approximate](https://asmedigitalcollection.asme.org/appliedmechanics/article/35/2/379/392117/A-Path-Independent-Integral-and-the-Approximate) doi: 10.1115/1.3601206
- 516 Ruina, A. (1983). Slip instability and state variable friction laws. *Journal of Geophysical
517 Research: Solid Earth*, 88(B12), 10359–10370. doi: 10.1029/JB088iB12p10359
- 518 Scholz, C. H. (2019). *The Mechanics of Earthquakes and Faulting* (3rd ed.). Cambridge
519 University Press. doi: 10.1017/9781316681473
- 520 Scholz, C. H., & Lawler, T. M. (2004). Slip tapers at the tips of faults and earthquake
521 ruptures. *Geophysical Research Letters*, 31(21), 1–4. doi: 10.1029/2004GL021030
- 522 Svetlizky, I., Albertini, G., Cohen, G., Kammer, D. S., & Fineberg, J. (2020). Dynamic
523 fields at the tip of sub-Rayleigh and supershear frictional rupture fronts. *Journal of
524 the Mechanics and Physics of Solids*, 137, 103826. doi: 10.1016/j.jmps.2019.103826
- 525 Svetlizky, I., & Fineberg, J. (2014). Classical shear cracks drive the onset of dry frictional
526 motion. *Nature*, 509(7499), 205–208. doi: 10.1038/nature13202
- 527 Svetlizky, I., Kammer, D. S., Bayart, E., Cohen, G., & Fineberg, J. (2017). Brittle Fracture
528 Theory Predicts the Equation of Motion of Frictional Rupture Fronts. *Physical Review
529 Letters*, 118(12), 125501. doi: 10.1103/PhysRevLett.118.125501
- 530 Uenishi, K., & Rice, J. R. (2003). Universal nucleation length for slip-weakening rupture
531 instability under nonuniform fault loading. *Journal of Geophysical Research: Solid
532 Earth*, 108(B1), 2042. doi: 10.1029/2001JB001681

- 533 Viesca, R. C., & Garagash, D. I. (2015). Ubiquitous weakening of faults due to thermal
534 pressurization. *Nature Geoscience*, 8(11), 875–879. doi: 10.1038/ngeo2554
- 535 Walsh, J. J., & Watterson, J. (1987). Distributions of cumulative displacement and seismic
536 slip on a single normal fault surface. *Journal of Structural Geology*, 9(8), 1039–1046.
537 doi: 10.1016/0191-8141(87)90012-5
- 538 Weng, H., & Ampuero, J. P. (2019). The Dynamics of Elongated Earthquake Ruptures.
539 *Journal of Geophysical Research: Solid Earth*, 124(8), 8584–8610. doi: 10.1029/
540 2019JB017684
- 541 Wu, B. S., & McLaskey, G. C. (2019). Contained Laboratory Earthquakes Ranging from
542 Slow to Fast. *Journal of Geophysical Research: Solid Earth*, 108(B1), 2019JB017865.
543 doi: 10.1029/2019JB017865